Check for updates

Advanced Functional Materials

ADVANCED FUNCTIONAL MATERIALS
www.afm-journal.de

RESEARCH ARTICLE OPEN ACCESS

Lithium Intercalation in the Anisotropic Van Der Waals Semiconductor CrSBr

Kseniia Mosina[1] | Aljoscha Söll[1] | Jiří Šturala[1] | Martin Veselý[2] | Petr Levinsky[3] | Ondřej Kaman[3] | Florian Dirnberger[4] | Giuliana Materzanini[5] | Nicola Marzari[6] | Gian-Marco Rignanese[5,7] | Borna Radatović[1,8] | Vlastimil Mazánek[1] | David Sedmidubský[1] | Zdeněk Sofer[1]

[1]Department of Inorganic Chemistry, Faculty of Chemical Technology, Technická 5, University of Chemistry and Technology Prague, Prague, Czech Republic | [2]Department of Organic Technology, Technická 5, University of Chemistry and Technology Prague, Prague, Czech Republic | [3]Institute of Physics of the Czech Academy of Sciences, Prague, Czech Republic | [4]Department of Physics, TUM School of Natural Sciences, Technical University of Munich, Garching, Germany | [5]Institute of Condensed Matter and Nanosciences (IMCN), Université Catholique de Louvain, Louvain-la-Neuve, Belgium | [6]Theory and Simulation of Materials (THEOS), and National Centre for Computational Design and Discovery of Novel Materials (MARVEL), École Polytechnique Fédérale de Lausanne (EPFL), Lausanne, Switzerland | [7]WEL Research Institute, Wavre, Belgium | [8]Centre for Advanced Laser Techniques, Institute of Physics, Zagreb, Croatia

Correspondence: Jiří Šturala (sturalaj@vscht.cz) | Martin Veselý (veselyr@vscht.cz) | Zdeněk Sofer (zdenek.sofer@vscht.cz)

Received: 1 September 2025 | **Revised:** 21 December 2025 | **Accepted:** 8 January 2026

Keywords: anisotropy | intercalation | layered magnets | lithium | van der Waals materials

ABSTRACT

Alkali metal intercalation is an important strategy for doping van der Waals materials. Lithium, in particular, was shown to achieve exceptional charge carrier densities, reaching levels at which fundamental electrical, optical, and magnetic material properties begin to be strongly modified. While lithium is known to be highly volatile, its migration dynamics in anisotropic layered crystals remain poorly understood. In this work, we investigate the intercalation of lithium between layers of the anisotropic magnetic semiconductor CrSBr. Using exfoliated crystals, we are able to monitor the dynamics of the intercalation process in real time through optical and electrical characterization methods. Our measurements reveal highly anisotropic migration of lithium characterized by diffusion coefficients that differ by more than one order of magnitude along *a*- and *b*-directions. This finding is in good agreement with our molecular dynamics simulations, which show trajectories of lithium atoms primarily follow the Br chains in the *a*-direction. Beyond that, we find that partially covering CrSBr crystals by thin hexagonal boron nitride (hBN) flakes has a significant impact on the intercalation process, and that lithium strongly enhances the electrical conductivity along the *a*-axis. Our method offers a new platform for lithium diffusion studies and encourages further research to pursue the fabrication of lithium-doped devices.

1 | Introduction

Lithium intercalation is one of the most powerful approaches for vastly tuning charge doping in layered semiconductors, magnets, and superconductors, and is traditionally accomplished via electrochemical methods [1–4]. Electrochemical intercalation plays a central role in many liquid-phase exfoliation protocols since it often induces bulk crystal delamination down to exfoliated flakes of high crystalline quality [5–8]. However, the fact that it relies on complex cell architectures limits in situ studies of intercalation into individual flakes. In contrast, chemical intercalation exploits the chemical potential of the intercalant as a

Kseniia Mosina and Aljoscha Söll contributed equally to this work.

This is an open access article under the terms of the Creative Commons Attribution License, which permits use, distribution and reproduction in any medium, provided the original work is properly cited.

© 2026 The Author(s). *Advanced Functional Materials* published by Wiley-VCH GmbH

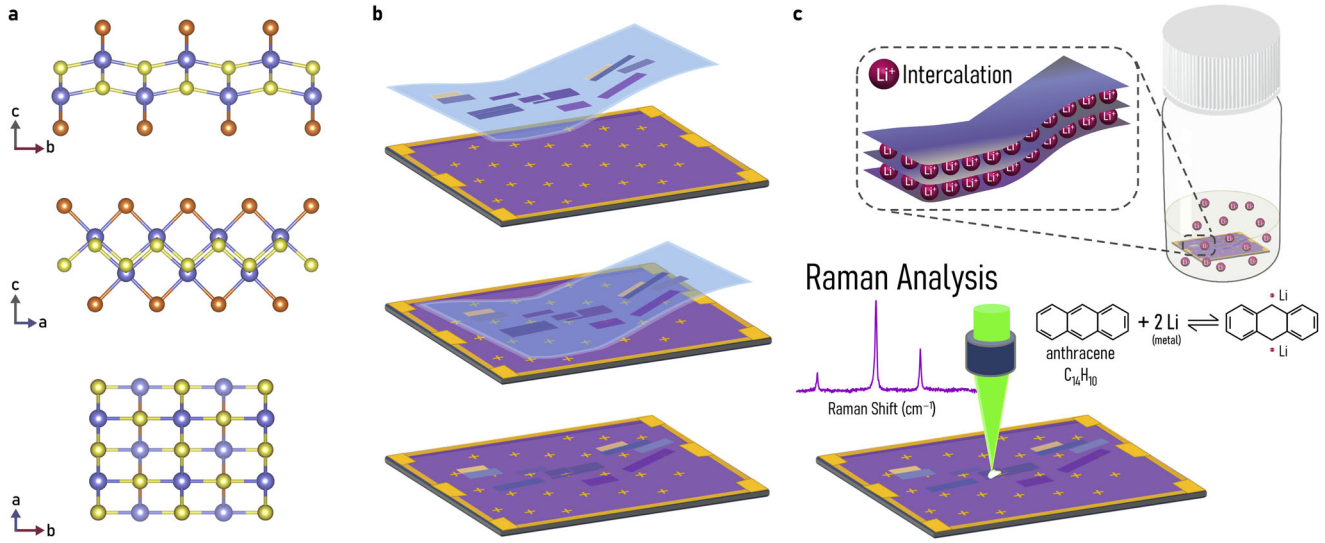

FIGURE 1 | Atomic model of CrSBr (a) with projection along the a-direction, b-direction, and c-direction. Structures are generated by VESTA software [21]. Schematic illustration of sample preparation starting with the mechanical exfoliation of CrSBr (b). Image (c) shows the process of lithium intercalation into exfoliated CrSBr, together with the schematic representation of lithium anthracenide formation in the presence of THF. The wafer with intercalated flakes is retrieved for Raman analysis.

driving force, bypassing the need for a working electrode or cell. This enables direct observation of individual flake lithiation on standard substrates (e.g., SiO_2/Si) and facilitates in situ optical and spectroscopic characterization [9]. Since the 1960s, chemical intercalation has been employed to investigate the effects of lithium intercalation on the electrical and magnetic properties of layered semiconductors such as FeOCl [10–12].

Another promising candidate for the study of lithium intercalation is the van der Waals magnetic semiconductor CrSBr. In its bulk state, CrSBr exhibits a direct band gap of 1.5 eV and an orthorhombic crystal structure of the *Pmmn* space group and D_{2h} point group [13]. Each layer of CrSBr consists of a covalently bonded network of Cr and S atoms, while Br atoms are bound exclusively to Cr atoms and arranged in chains along the *a*-direction (Figure 1a) [14]. This distinctive atomic arrangement leads to significant structural anisotropy, evidenced by distinct lattice constants along the crystallographic axes (a = 3.506 Å, b = 4.767 Å, and c = 7.965 Å) [14]. The relatively weak interlayer hybridization facilitates an easy cleavage of layers when exfoliating the material, resulting in rectangular sheets elongated in the *a*-direction due to the in-plane bonding anisotropy.

CrSBr has garnered considerable attention in the past few years because of its anisotropic electronic transport and distinctive magnetic behavior with A-type antiferromagnetic ordering below T_N ≈132 K and ferromagnetism in the monolayer [15, 16]. The magnetic ground state in layered van der Waals magnets is known to be highly sensitive to the presence of guest species, as demonstrated by substantial changes in critical temperature for magnetic order, magnetic anisotropy, and even the type of magnetic order in intercalated Fe_xTaS_2 [17], $Fe_{3-x}GeTe_2$ [18], and several other van der Waals magnets [19]. Feuer et al. recently showed that lithium intercalation similarly has a profound impact on bulk CrSBr, transforming it from an antiferromagnet into a ferromagnet with an enhanced Curie temperature of T_C ≈ 200 K, along with pronounced triaxial magnetic anisotropy and an increased saturation magnetization per Cr atom [20]. They further observed the emergence of a charge density wave state and demonstrated a substantial increase in conductivity in the *a*-direction due to charge carrier doping. While all studies in the aforementioned work were conducted on intercalated bulk material, the importance of studying exfoliated samples was also highlighted. For example, thin flakes would allow single-crystal magnetization measurement and direct transport measurements in the *b*-direction that are hindered by grain boundary and defects formation in bulk Li-CrSBr [20].

Here, we identify optimal conditions for the intercalation of lithium ions by monitoring their spatiotemporal dynamics in exfoliated CrSBr crystals in situ using Raman spectroscopy and electrical transport measurements. Additionally, we show that partial or complete hBN encapsulation strongly affects the dynamics and in-plane anisotropy of Li^+ diffusion. Conductance measurements confirm the feasibility of studying charge transport along both the *a*- and *b*-directions, while magnetic susceptibility data from liquid-phase exfoliated flakes demonstrate the emergence of a ferromagnetic ground state. These results establish our method as a practical platform for the intercalation of pre-fabricated structures, paving the way for future device applications and single-flake magnetic studies that were previously restricted to the bulk.

2 | Results and Discussion

2.1 | Lithium Intercalation in Exfoliated CrSBr

We present a lithium intercalation method for exfoliated CrSBr, schematically illustrated in Figure 1b,c. To begin, we prepare the sample of mechanically exfoliated CrSBr transferred onto an Si/SiO_2 wafer using the conventional Scotch tape method (see Methods) and characterize CrSBr flakes by optical microscopy, atomic force microscopy (AFM), and Raman spectroscopy prior

16163028, 0, Downloaded from https://advanced.onlinelibrary.wiley.com/doi/10.1002/adfm.202523178 by Gian-Marco Rignanese - <shibboleth-member@uclouvain.be> , Wiley Online Library on [17/02/2026]. See the Terms and Conditions (https://onlinelibrary.wiley.com/terms-and-conditions) on Wiley Online Library for rules of use; OA articles are governed by the applicable Creative Commons License

to intercalation. Optical contrast of the flakes is correlated with AFM-measured thickness, and the characteristic A_g^1, A_g^2, A_g^3 vibrational modes of CrSBr at 114, 244, and 342 cm^{-1}, respectively, are confirmed via Raman spectroscopy (see Section S1). To initiate intercalation, the sample is immersed in a lithium anthracenide solution in tetrahydrofuran (THF), as shown in Figure 1c. Further details on solution preparation are provided in the Methods and Figure S2. During the intercalation process, anthracene in its reduced ionic form donates one electron to the CrSBr structural unit, reducing chromium from the formal oxidation state Cr(III) to Cr(II). As the structure must remain charge-neutral, the excess electrons are compensated by positively charged lithium cations intercalating into CrSBr. After intercalation, the sample of Li-CrSBr is rinsed with dry THF and characterized by Raman spectroscopy again, which serves as an effective tool for real-time monitoring of lithiation. To confirm that lithium is indeed intercalated between van der Waals layers rather than accumulating on the surface, we employ time-of-flight secondary-ion mass spectrometry (TOF-SIMS). The technique described in more detail in Section S2 demonstrates that after intercalation, lithium ions are distributed across CrSBr layers.

To identify suitable intercalation conditions, we test a range of lithium anthracenide concentrations (see Section S3). We find that a minimum concentration of 0.2 mM is required to initiate intercalation within 15 min. Increasing the concentration further accelerates the process but risks damaging thin flakes. Signs of deterioration can be observed at 0.64 mM (Figure S8). A concentration of 0.32 mM thus offers an optimal balance between intercalation efficiency and preservation of the crystal structure. In the experiment, this corresponds to a concentration at which the initially blue lithium anthracenide solution turns colorless during the dilution with dry THF. Hence, it is straightforward to control.

To investigate the effect of intercalation on vibrational Raman modes, we repeatedly intercalate a ≈6 nm CrSBr flake with lithium anthracenide solution (0.32 mM in THF) in 3 min intervals, acquiring Raman spectra and optical images after each interval, as presented in Figure 2a,b. The resulting spectra reflect changes in the lattice parameters driven by the insertion of lithium ions into CrSBr. Upon intercalation, Raman spectra reveal two distinct sets of phonon modes, A_g and A_1, indicating the presence of both intercalated and non-intercalated material within the area we probe. As intercalation proceeds, A_g modes gradually diminish and new A_1 modes emerge at lower frequencies, reflecting the reduction in symmetry from D_{2h} to C_{2v} in Li–CrSBr, as shown in Figure S9.

Within the first 3 min, the onset of A_1^1 and A_1^2 modes respectively appear at 100 cm^{-1} and at about 220–230 cm^{-1}. The A_g^3 mode broadens slightly with an asymmetric low-energy tail. At 6 min, the A_1^1 mode intensity increases, while the A_g^1 mode of pristine CrSBr softens yet persists at 114 cm^{-1}, and further broadening is observed of both A_g^2 and A_g^3 peaks. After 9 min, the A_1^1 mode becomes dominant, and a broadened A_1^2 feature reflects evolving phonon interactions associated with Li-CrSBr. At 12 min, intercalation is complete, as all A_g modes from the pristine material vanish, and A_1 modes are fully developed. Extending the time to 15 min yields no further changes, indicating completion of lithiation in the ≈6 nm CrSBr flake within 12 min. Despite these spectral changes that confirm intercalation, there are no evident changes in the optical contrast of the flake. Because the flake is only about 6 nm thick and intercalation increases its height by only a few nanometers, this difference is not apparent in standard optical micrographs without more advanced RGB analysis (Figure 2a) [22]. We repeat the experiment with another flake to demonstrate how the intensity of each mode depends on the laser polarization (Figure 2c). The pristine flake shows the expected polarization dependence for CrSBr with the A_g^1 and A_g^3 mode most intense for excitation polarization parallel to the *b*-direction E||*b* and the A_g^2 mode most intense for E||*a*. After intercalation, this trend is mostly maintained, however, A_1^2 and A_1^3 show a weaker dependence, and their intensity does not decrease

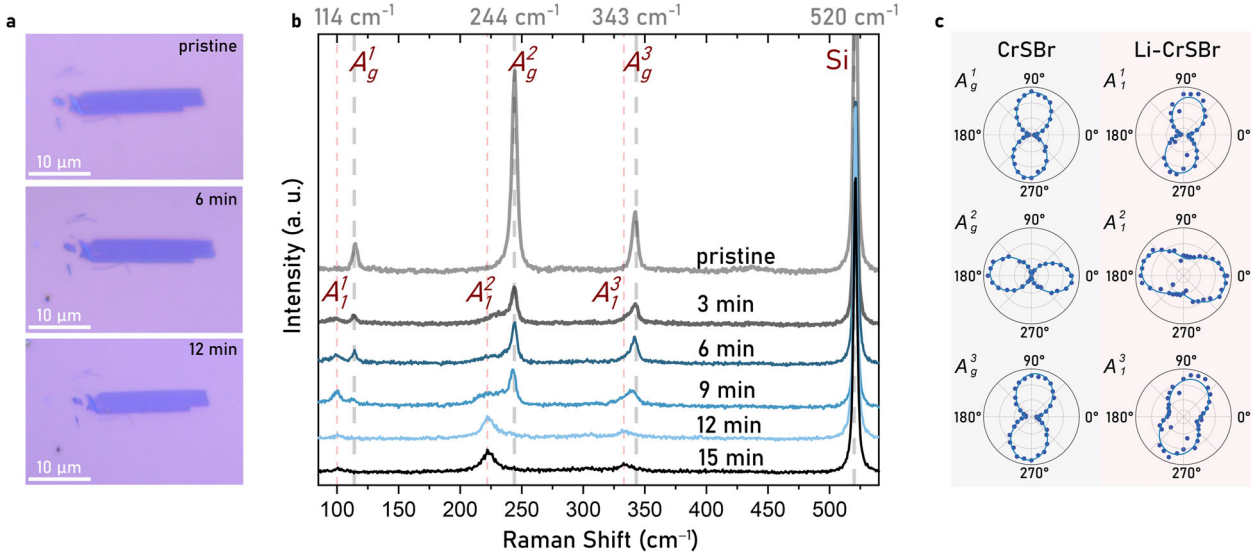

FIGURE 2 | (a) Optical micrographs of exfoliated flakes upon intercalation evolution. (b) Corresponding time-resolved Raman spectra of a CrSBr flake collected upon intercalation. (c) Polarization dependence of Raman modes for a pristine and an intercalated flake. The dependence becomes less pronounced while the general trend is maintained.

16163028, 0, Downloaded from https://advanced.onlinelibrary.wiley.com/doi/10.1002/adfm.202523178 by Gian-Marco Rignanese - <shibboleth-member@uclouvain.be> , Wiley Online Library on [17/02/2026]. See the Terms and Conditions (https://onlinelibrary.wiley.com/terms-and-conditions) on Wiley Online Library for rules of use; OA articles are governed by the applicable Creative Commons License

TABLE 1 | Calculated and observed Raman shifts related to a displacement of selected atoms.

	CrSBr			Li-CrSBr	
	Theory / cm^{-1}	**Exp. / cm^{-1}**		**Theory / cm^{-1}**	**Exp. / cm^{-1}**
A_g^1	116.2	114	A_1^1	92.3	95
A_g^2	241.0	244	A_1^2	206.5	219
A_g^3	332.1	342	A_1^3	328.6	331

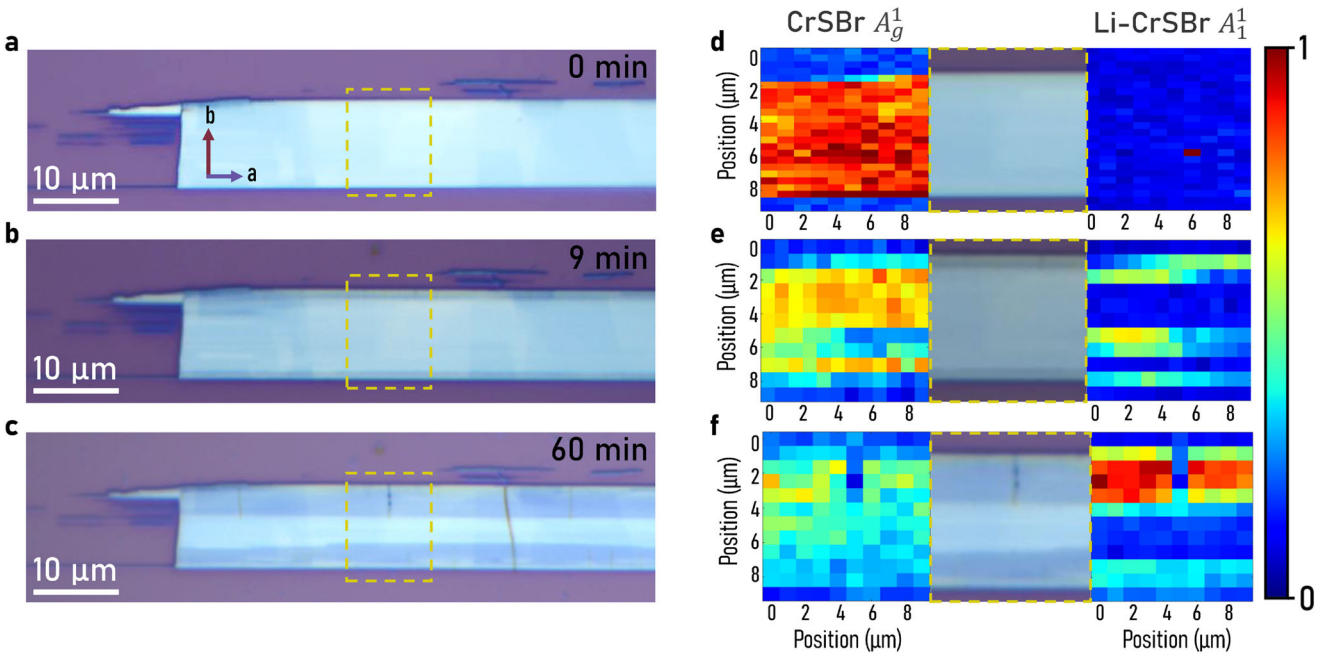

FIGURE 3 | Optical micrographs captured at (a) 0 min, (b) 9 min, and (c) 60 min of intercalation. The yellow rectangle in each optical image indicates the specific area chosen for mapping. (d-f) The peak intensity maps of $\boldsymbol{A}_g^1$ and $\boldsymbol{A}_1^1$ modes collected at corresponding time intervals.

all the way to zero, which could be attributed to a disorder starting to appear within the structure.

To support our findings in the Raman study, we perform density functional theory (DFT) calculations (see Methods for further details). In pristine CrSBr, the calculated A_g^1, A_g^2, and A_g^3 modes align well with experimental values. Upon intercalation, symmetry and peak assignment change, resulting in a structure $CrSBrLi_{0.5}$ similar to $FeOClLi_x$ [10]. The theoretical positions of the A_1^1, A_1^2, A_1^3 modes show good agreement with experiment (see Table 1). Atomic displacements are shown in Figure S9. The A_1^3 mode is the least affected by lithium intercalation, since that peak originates from Cr and S displacements and its position is not determined with high precision computationally.

To get a better understanding of the intercalation process, we examine the intercalation of a CrSBr flake with a thickness of about 50 nm. The sample is intercalated in the same manner as described above, and the progression of intercalation over time is monitored. We track the spatial distribution of the A_1^1 mode signal intensity at 95 cm^{-1} and compare it directly with the A_g^1 mode at 114 cm^{-1}. Figure 3 shows the optical images during lithiation, along with corresponding peak intensity maps of the A_g^1 and A_1^1 modes. The optical image of the pristine flake is shown in Figure 3a. As expected, the A_1^1 mode of Li–CrSBr is absent, while the A_g^1 mode of CrSBr shows a strong, uniform signal (Figure 3d). After 9 min, the A_1^1 mode emerges prominently, visualized by high-intensity stripes along the flake edges, while the A_g^1 signal weakens, especially at the boundaries, indicating edge-initiated, partial intercalation, which slowly spreads inward (Figure 3e). After 60 min, the intercalated region is clearly visible in the optical micrograph (dark blue stripes in Figure 3c), and the A_1^1 mode dominates the Raman response (Figure 3f), confirming progressive lithiation of the flake. Furthermore, to understand intercalation-induced changes in the CrSBr topography, we investigate two flakes with different thicknesses before and after intercalation via atomic force microscopy, as shown in Figures S10 and S11 and elaborated in detail in Section S4. For both flakes, we observe an increase in thickness of around 50% relative to their initial height. For the thinner flake, which we intercalated completely, we do not observe any change in the Li^+ distribution after 12 days under an inert atmosphere, as shown in Figure S10. In contrast, for the thicker flake, which we intercalated only partially, we observe that the edges initially accumulate an excess of Li^+ while the center remains mostly pristine, giving rise to a Li^+ concentration gradient across the flake. During subsequent equilibration over the following days, Li^+ diffuses toward the center of the flake, gradually homogenizing the concentration

16163028, 0, Downloaded from https://advanced.onlinelibrary.wiley.com/doi/10.1002/adfm.202523178 by Gian-Marco Rignanese - <shibboleth-member@uclouvain.be> , Wiley Online Library on [17/02/2026]. See the Terms and Conditions (https://onlinelibrary.wiley.com/terms-and-conditions) on Wiley Online Library for rules of use; OA articles are governed by the applicable Creative Commons License

profile, leading to a decrease in the edge thickness and an increase in the thickness of the center, as shown in Figure S11.

At first glance, our observations presented in Figure 3 seem to suggest that intercalation occurs exclusively along the *b*-axis. From a microscopic point of view, however, one could argue that the anisotropic atomic arrangement of Cr-Br chains along the *a*-direction creates a unique bonding situation [13], which should facilitate an easy diffusion of guest ions along the *a*-direction. It lowers the migration energy barrier, creating diffusion channels within the structure, which should dictate the diffusion mechanism. Therefore, we propose that lithium ions are unable to enter the material from the short edge (perpendicular to the *a*-direction). Instead, they enter from the long edge (perpendicular to the *b*-direction), where they rapidly spread through the diffusion channels oriented along the *a*-direction, and the intercalation only gradually progresses inward along the *b*-direction, leading to the observations in Figure 3a–c.

We test this hypothesis in a series of intercalation experiments with fully or partially hBN encapsulated CrSBr. Initially, we confirm that fully encapsulating pristine CrSBr in hBN protects it from intercalation entirely (Figure S13a–c). Then, we cover the CrSBr partly either along the *a* or *b*-direction, leaving one part exposed for lithium entry. When hBN coverage leaves an exposed edge perpendicular to the *b*-axis, intercalation progresses slowly inward along the *b*-direction from this exposed edge, similar to a non-encapsulated flake (Figure S14b). In contrast, when the exposed edge is perpendicular to the *a*-axis, lithium enters and then quickly spreads underneath the hBN-covered area along the *a*-direction (Figure S13d–f), suggesting that Li^+ diffusion is indeed significantly faster along the *a*-direction.

To get an estimate for the anisotropy ratio of diffusion coefficients, D_a/D_b, we partially encapsulate a sheet of CrSBr with a thickness of about 25 nm in hBN along the *a*-direction, as shown in Figure 4b, and intercalate it in multiple 30–60 s intervals. After each intercalation step, we track the progress of intercalation deep within the hBN-covered area based on the optical contrast. Figure 4a shows how diffusion progresses for a selected area. Under the assumption of 1D diffusion in each direction, we can gain an estimate for the diffusion coefficient according to $L^2 = 2Dt$ [23–25]. In Figure 4c, we present the progression of intercalation in the selected area as L^2 vs. t for one diffusion length measurement in each direction for each time step (further details are found in Section S6). We notice immediately that intercalation along the *a*-direction proceeds markedly faster, as evidenced by the steeper slope. Additionally, we observe two distinct regimes, a slow initial diffusion followed by accelerated diffusion, which is likely triggered by a lattice parameter change that facilitates faster ion transport. We calculate an average anisotropy ratio of the diffusion coefficients of $D_a/D_b \approx 21.8 \pm 1.1$. Similar anisotropy of Li^+ diffusion has been reported for the in-plane anisotropic GeP during electrochemical lithium intercalation with a ratio of $D_a/D_b \approx 25$ [25].

To further clarify the diffusion mechanism, we perform *NVT ab initio* molecular dynamics (AIMD) simulations (~50 ps) at four temperatures ranging from 600 to 1200 K on a Li-intercalated periodic CrSBr supercell containing 80 atoms, corresponding to 11% lithium intercalation (see Section S7). In the supercell, the *x*, *y*, and *z* parameters correspond to *a*, *b*, and *c* lattice axis of CrSBr, respectively.

To quantify the diffusion anisotropy, we compute direction-resolved lithium mean squared displacements (MSD) from the Li-ion trajectories (inset in Figure 4c; Figure S19i–l), clearly revealing the dominance of the *x*-component. Importantly, the non-zero *z*-component does not imply that lithium ions are diffusing through the sheets in the *z*-direction. Instead, it corresponds to vertical ion movements required to access neighboring *x*-direction diffusion channels, as depicted schematically in the structural inset in Figure 4c and reported in the simulated Li-ion trajectories in Figure S18b (see also Videos S1–S6). Using the time-averaged Einstein relation (see Section S7 and Refs [26–30].), we estimate the total (Figure S20) and direction-resolved (Figure S21) self-diffusion coefficients at the four temperatures, obtaining a theoretical D_x/D_y ratio of 20.7 ± 7.2 at 600 K, which is in good agreement with the experimental value. The large uncertainty in the theoretical D_x/D_y ratio arises from the very small value of D_y, which leads to a significant statistical error (see Figure S21). Above 600 K, D_x/D_y ratio decreases significantly to 6.5 ± 3.3 at 800 K, followed by a more gradual reduction at higher temperatures, suggesting that the *y*-channels begin to open above 600 K. This trend is also evident in the Arrhenius plot for Li^+ diffusion (Figure S22). The more pronounced change in the D_x/D_y ratio between 600 and 800 K, compared to the smaller variation between 800 and 1200 K, may indicate the presence of two distinct diffusion regimes, with a discontinuous transition occurring between 600 and 800 K, and a smoother evolution of anisotropy at temperatures below and above this range.

2.2 | Effect of Lithium Intercalation on Magnetic Properties of Exfoliated CrSBr

To demonstrate that our intercalation method modifies the magnetic properties of exfoliated CrSBr, we applied lithium intercalation to liquid-phase exfoliated flakes obtained by sonication of bulk CrSBr in NMP (see Section S8), yielding CrSBr flakes tens to hundreds of layers thick (Figure S23a). Following intercalation with lithium anthracenide, the resulting Li-CrSBr flakes exhibit a magnetic susceptibility indicative of the transformation from an antiferromagnetic ground state ($T_N \approx 134$ K) to a ferromagnetic one with $T_C \approx 190$ K (Figure S23c). Magnetization loops reveal the emergence of hysteretic behavior in Li-CrSBr, and the Curie–Weiss fit indicates enhanced ferromagnetic interactions (Figure S24). These results establish a foundation for future single-flake magnetic studies, where anisotropic CrSBr flakes can be probed without the limitations of bulk samples.

2.3 | Effect of Intercalation on Electronic Properties of Exfoliated Sheets

A previous study on lithium intercalation of bulk CrSBr crystals found a significant increase in conductivity when measuring along the *a*-direction, while high resistance due to grain boundaries or poor contacts impeded measurements along the *b*-direction [20]. We fabricate a six-terminal device to study the direction-dependent conductance of exfoliated few-layer sheets before and after intercalation. Furthermore, we investigate how

16163028, 0, Downloaded from https://advanced.onlinelibrary.wiley.com/doi/10.1002/adfm.202523178 by Gian-Marco Rignanese - <shibboleth-member@uclouvain.be> , Wiley Online Library on [17/02/2026]. See the Terms and Conditions (https://onlinelibrary.wiley.com/terms-and-conditions) on Wiley Online Library for rules of use; OA articles are governed by the applicable Creative Commons License

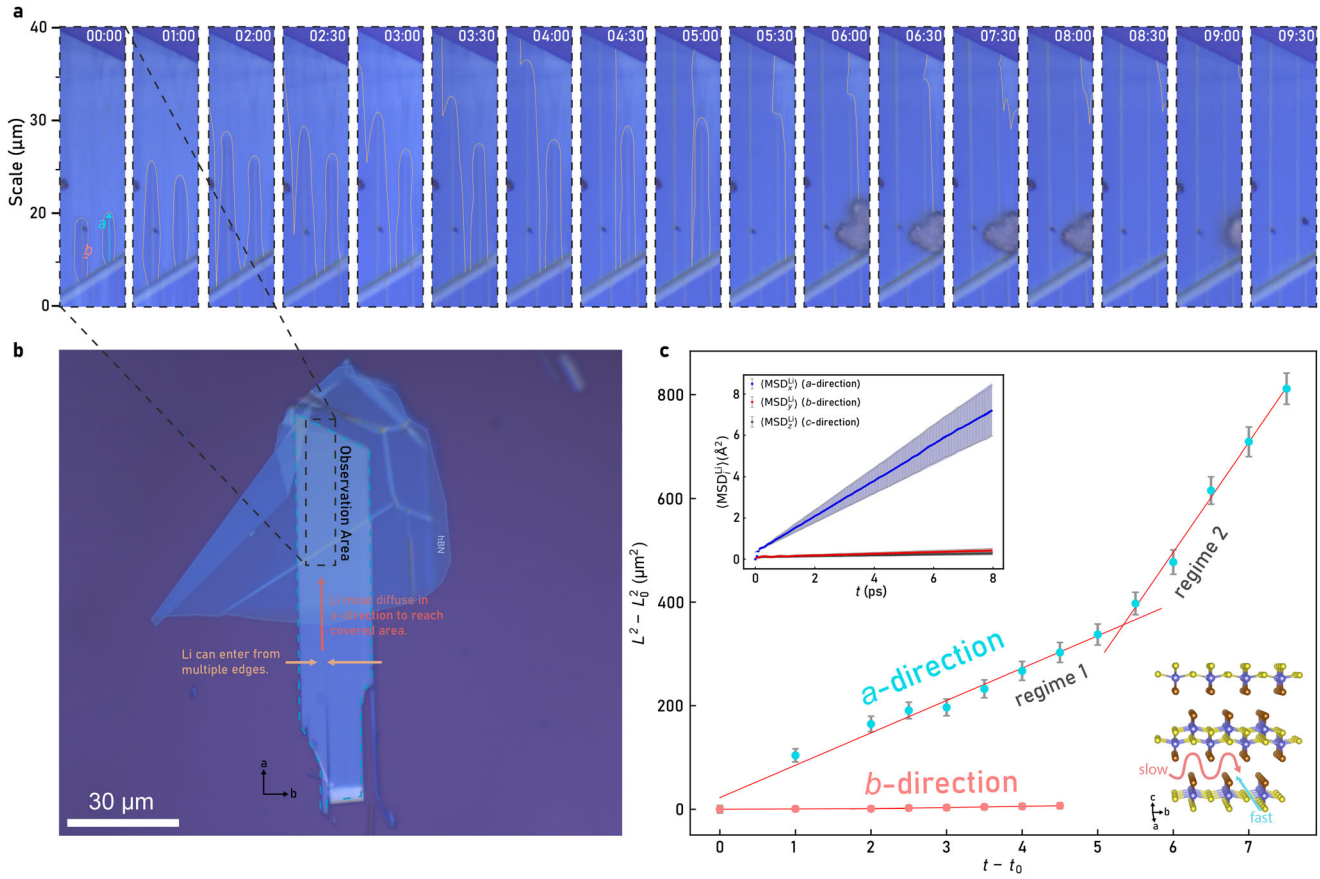

FIGURE 4 | (a) Progression of Li^+ diffusion within the covered area of a partially hBN encapsulated sheet of CrSBr. A yellow line was added to easily distinguish the border between CrSBr and Li-CrSBr. To indicate the positions where the diffusion length is tracked, two arrows are added to the first panel for either direction, marked *a* and *b*. The gray particle seen between 06:00 and 08:00 is a lithium salt, which briefly deposited on the structure and was later washed away. (b) Optical micrograph of the whole heterostructure. The upper part is covered by hBN, the lower part is uncovered. During the intercalation, lithium can only enter the sheet from the exposed area and then diffuse into the covered part along the *a*-direction, until it reaches the observation area marked by the dashed line. (c) Plot of the diffusion progress as the relative increase of the square of diffusion length ($L^2 - L_0^2$) vs. $t - t_0$. The structure of CrSBr is shown on the bottom-right with the two diffusion directions marked by arrows. The inset in the top-left shows the computed direction-resolved lithium mean squared displacements at 600 K for comparison.

the properties change over time when the device is exposed to air. The optical micrograph in Figure 5a shows the six-terminal device before and after intercalation as well as after 30 h of measurement in air. We conclude it was fully intercalated from the Raman measurements in Figure 5c taken in the middle of the device. The contact configuration allows us to simultaneously study the effect of intercalation in either crystal direction on the same device, by continuously measuring *I*–*V* sweeps along the two in-plane directions.

Figure 5b shows the temporal evolution of the static two-terminal conductance G_{2T} at 1.0 V, along *a*- and *b*-directions, extracted from the repeated *I*–*V* sweeps. Initially, it is constant, around 0.6 µS for pristine CrSBr in both directions. Upon intercalation, the measurement is repeated in air, and we immediately observe a sharp increase in G_{2T} in the *a*-direction reaching around 0.9 µS. Subsequently, it decreases over a duration of 30 h and approaches a constant value of 0.4 µS. Along the *b*-direction, on the other hand, G_{2T} never exceeds the pristine value. Instead, it drops slightly immediately after intercalation and then follows a similar trend of steady decrease as observed in the *a*-direction, eventually reaching a constant value of 0.3 µS. Multiple *I*–*V* curves for each direction taken during the 30-h measurement are shown in Figure 5d,e, additionally Figure S26 shows only the initial 40 min in more detail. In both directions, the initially nearly linear *I*–*V* curves show a pronounced non-linearity immediately after the intercalation.

We propose that two opposing effects are at play during the initial part of the measurement. In the ideal case, the intrinsic conductivity of Li-CrSBr is higher than that of CrSBr as a result of lithium donating electrons to CrSBr during the intercalation, which raises the Fermi level and leads to additional charge carriers present in the conduction bands [20]. From this effect, we would expect to observe a substantial increase in conductance. At the same time, however, the intercalation may increase contact resistance and introduce carrier-injection barriers at the Au–Li-CrSBr interface, consistent with Schottky-type or tunneling-limited injection. This can have mechanical causes, like the solvent partially lifting the sheet and reducing the effective contact area. More generally, intercalation-induced expansion has been reported to mechanically compromise metal contacts and electrodes [31]. Alternatively, it could arise from interfacial residue formed during the intercalation, leading to nonlinear

16163028, 0, Downloaded from https://advanced.onlinelibrary.wiley.com/doi/10.1002/adfm.202523178 by Gian-Marco Rignanese - <sbibobeth>-member@uclouvain.be , Wiley Online Library on [17/02/2026]. See the Terms and Conditions (https://onlinelibrary.wiley.com/terms-and-conditions) on Wiley Online Library for rules of use; OA articles are governed by the applicable Creative Commons License

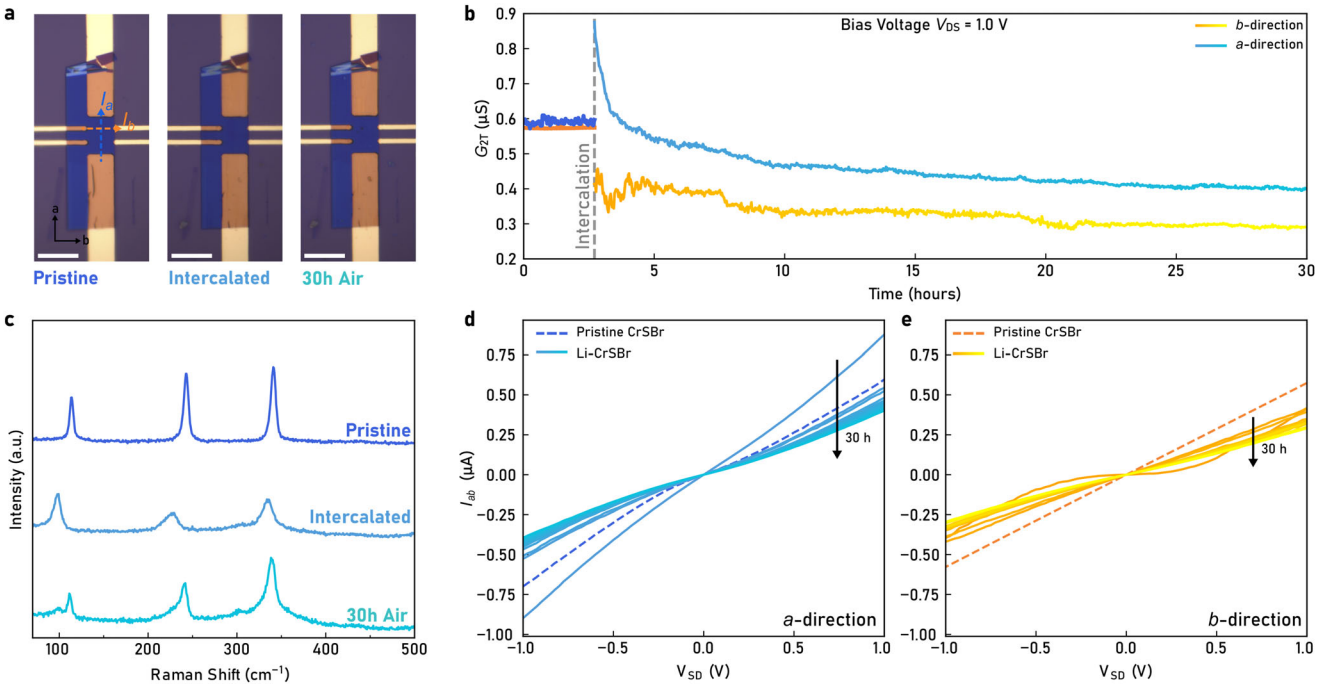

FIGURE 5 | (a) Optical Micrographs of the CrSBr device before intercalation, after intercalation, and after 30 h of *I–V* sweeps. (b) Time dependence of static two-terminal conductance G_{2T} before and after intercalation. G_{2T} was extracted from the *I–V* sweeps at a bias of 1.0 V ($G_{2T} = I(V_{DS} = 1\,V)/1\,V$). (c) Raman spectra of the pristine and intercalated device and after 30 h of measurements (taken in the middle of the device). (d-e) *I–V* sweeps in the *a*- and *b*-directions at different times over a period of 30 h.

I–V characteristics and a reduction in measured G_{2T}. In the *a*-direction, G_{2T} still increases overall, consistent with an intrinsic conductivity enhancement of Li-CrSBr. In contrast, along the *b*-direction G_{2T} remains below the pristine value, suggesting additional limitations beyond residue effects or partial lifting of flakes. One possible contribution is micro-delamination or line defects, which would segment the flake into narrow ribbons aligned in *a* and preferentially impede transport along *b*, while leaving *a*-direction transport less affected. AFM measurements in Figure S12 show such line-like features, consistent with microscopic tears. The modest recovery observed in *b* during the first hours is consistent with partial relaxation of the interface or current-induced annealing [32, 33], although the persistent *I–V* curvature indicates that injection-limited transport remains important.

The following general decrease in conductance over time observed for both directions shows that Li-CrSBr is not air stable and will gradually lose its lithium, most likely through reaction with moisture in the air. The third Raman spectrum (30 h Air) in Figure 5c confirms that after 30 h in air, the intercalation has been almost completely reversed, which is indicated by the reappearance of pristine Raman modes with only small shoulders remaining. This deintercalation process appears to happen uniformly as both curves follow a similar trajectory for most of the measurement. Further measurements (Section S9) confirm this trend of gradual deintercalation upon exposure to air.

Furthermore, we have inspected the long-term stability of Li-CrSBr devices when kept in an inert atmosphere. As shown in Figures S26 and S27, following the initial change in conductance right after intercalation, the performance remains stable over days or even weeks, and the gradual decrease due to deintercalation is not seen under these conditions.

3 | Conclusion

Our work demonstrates that lithium can be intercalated into exfoliated CrSBr. This process is highly anisotropic, which is in good agreement with atomistic simulations. We tracked the intercalation dynamics by leveraging Raman spectroscopy, optical contrast, and electrical transport measurements and revealed that lithium intercalation serves as an effective tool for tuning the electronic and magnetic properties of CrSBr. The ability to intercalate lithium in a controlled manner by using partial hBN encapsulation establishes a robust platform for investigating alkali metal intercalation into layered 2D materials, offering new opportunities for tailoring the properties of van der Waals materials for future applications in electronics, energy storage, and quantum materials research.

4 | Experimental Section

4.1 | Exfoliated CrSBr Sample Fabrication

CrSBr bulk crystals were synthesized by chemical-vapor transport (CVT) as described in ref. [8]. We employed a conventional Scotch tape method to exfoliate bulk CrSBr and transfer exfoliated material on top of Si/SiO_2 substrates to conduct optical microscopy and Raman spectroscopy studies. All studies described in this paper were conducted on the SiO_2 (300 nm)/p^+ Si substrates. To meet the requirements of the secondary ion mass spectrometry

16163028, 0, Downloaded from https://advanced.onlinelibrary.wiley.com/doi/10.1002/adfm.202523178 by Gian-Marco Rignanese - <sbibobeib--member@uclouvain.be> , Wiley Online Library on [17/02/2026]. See the Terms and Conditions (https://onlinelibrary.wiley.com/terms-and-conditions) on Wiley Online Library for rules of use; OA articles are governed by the applicable Creative Commons License

method, we prepared gold-coated (250 nm) Si/SiO_2 substrates by metal evaporation and transferred exfoliated flakes simply by the Scotch tape method. For electronic characterization of CrSBr devices, the CrSBr was exfoliated on polydimethylsiloxane (PDMS) and transferred via the common PDMS dry transfer method. For this purpose, the glass slide was loaded into the prober arm of the transfer setup, and the flake was transferred onto a Si/SiO_2 substrate with prefabricated gold electrodes. The stage was heated to 60 °C, maintained at that temperature for 30 s, and then the glass slide was slowly lifted. For hBN/CrSBr heterostructures, a slightly different pickup and dry transfer method was employed. A thick PDMS sheet was cut into the shape of a pyramid and covered with a thin layer of polycarbonate (PC), which was obtained by drop casting a 7 wt.% solution of PC in chloroform between two glass slides and letting the solvent evaporate in air. The PDMS stamp was loaded into the prober arm of the transfer setup and used to pick up exfoliated hBN from PDMS at 90 °C. Subsequently, the CrSBr flake was picked up through van der Waals interactions with the hBN sheet on the PC stamp. Finally, the heterostructure was released on a SiO_2/Si substrate with prefabricated gold electrodes at 185 °C. The remaining polymer was dissolved by submerging the device in chloroform for 2 h at room temperature. All transfers were carried out in an argon atmosphere to avoid sample degradation. All devices were annealed to improve their electrical performance (5 h, 300 °C, 10^{-6} mbar).

4.2 | Lithium-Solvated Electron Solution

Lithium anthracenide stock solution was prepared in the following way: Anthracene (77.40 mg, 0.4340 mmol) is first dissolved in dry THF (4.55 mL) followed by the reaction with metallic lithium (2.00 mg, 0.288 mmol) under an inert argon atmosphere. The brilliant blue color of the resulting solution immediately arises from the presence of radical anions. Lithium anthracenide stock solution molarity is 32 mM. Note that we would like to keep anthracene in excess to make sure the limiting factor is not the availability of anthracene. The dry solvent is ultimately necessary since even traces of water or oxygen will destroy the radical reagent. Under careful observation, we exposed the reaction mixture to gentle manual shaking without stirring until the reaction was complete, which was manifested by a deep blue color and no traces of metallic lithium on the surface. Therein, the prepared stock solution was kept at a cooling temperature of −30 °C. To make the solution suitable for intercalation, it needs to be diluted with dry THF by a factor of ∼100 to reach a concentration of approximately 0.32 mM. The exact dilution factor may vary, e.g., due to residual moisture in the reagents, so we suggest monitoring the color of the solution during the dilution process. The point where the bluish hue has just vanished, and the solution is colorless, usually corresponds to a concentration well suited for intercalation.

4.3 | Characterization Methods

Ambient-condition current measurements were carried out at room temperature with a six-channel Keysight B1500 Precision Source/Measure Unit (SMU) in an INSTEC 4-probe measurement setup. Raman spectral measurements and mapping were conducted with a WITec Confocal Raman Microscope (WITec alpha300 R, Ulm, Germany), equipped with a 532 nm laser and a spectrometer with a thermoelectrically cooled CCD camera sensor. The measurements were performed in an argon-filled glovebox at room temperature with a 100× objective and a laser power of less than 2.5 mW to avoid sample degradation. Characterization by AFM was performed on a NanoMagnetics ezAFM compact AFM system in dynamic mode (tapping mode) inside an argon-filled glovebox. Temperature-dependent conductivity measurements were performed using the Electrical Transport Option (ETO) of the Physical Property Measurement System (PPMS) instrument manufactured by Quantum Design.

4.4 | Raman Mapping

Raman spectra were pre-processed in MATLAB (R2024a) to enhance signal quality and remove background contributions. Raw intensity data were first smoothed using a second-order Savitzky–Golay filter (mssgolay in-built MATLAB function) with a span of 7 points to suppress random noise while preserving peak features. Subsequently, each spectrum baseline was corrected by segmenting the spectrum into equal-width windows and estimating local baselines within each window using a 10th percentile of the intensity distribution. These local baseline points were then interpolated across the spectrum using a smooth spline to model the global background (msbackadj in-built MATLAB function), which is subtracted from the original spectrum. For quantitative analysis, the A_g^1 mode was integrated over the spectral range of 104–126 cm^{-1}, while the A_1^1 mode was integrated over 91–105 cm^{-1}.

4.5 | DFT Phonon Calculations

To verify our Raman shifts and the structure, we optimized the CrSBr and CrSBr-Li unit cell structure, including the atom positions in the QUANTUM ESPRESSO software package [34 #adfm74033-bib-0035">34, 35], rev 7.1. The unit cell of CrSBr consisted of two Cr, two S, and two Br atoms; Li-CrSBr contained also one Li atom (a similar structure was also proposed for FeOCl-Li [10]). The PBE functional was used for all calculations with the projector-augmented wave method (PAW) obtained from the PSEUDOJO library [36] with a wavefunction kinetic energy cutoff $E_{cut} = 50$ Ry and a charge density energy cutoff $E_{cut} = 500$ Ry. The convergence criteria for the cell optimization were: energy $<10^{-6}$ Ry, force $<10^{-4}$ Ry/Bohr. The required SFC convergence was set to $<10^{-15}$ Ry. Requested k-spacing 0.15 $Å^{-1}$, leading to $12 \times 9 \times 6$ mesh, was used. Phonon modes were calculated at the Γ point.

4.6 | Sample Preparation for Magnetic Measurements

To probe the magnetic properties of Li-intercalated CrSBr, we prepared liquid-phase exfoliated CrSBr for subsequent intercalation with lithium anthracenide. Briefly, 30 mg of bulk CrSBr was ground in an agate mortar to reduce the crystal size and facilitate liquid-phase exfoliation. The ground material was then dispersed in 30 mL of anhydrous *N*-methyl-2-pyrrolidone (NMP, Sigma-Aldrich, 99.5%) and subjected to sonication-assisted liquid-phase

16163028, 0, Downloaded from https://advanced.onlinelibrary.wiley.com/doi/10.1002/adfm.202523178 by Gian-Marco Rignanese - <shibboleth-member@uclouvain.be> , Wiley Online Library on [17/02/2026]. See the Terms and Conditions (https://onlinelibrary.wiley.com/terms-and-conditions) on Wiley Online Library for rules of use; OA articles are governed by the applicable Creative Commons License

exfoliation using a horn sonicator. The dispersion was sonicated for 40 min at an amplitude of 20%, corresponding to a total applied energy of approximately 68 kJ, while maintaining the temperature at 18 °C using a water chiller. Following sonication, the dispersion was subjected to a size-selection procedure by centrifugation at 241 rcf for 20 min to remove unexfoliated CrSBr. The supernatant containing exfoliated flakes was then centrifuged at 10000 rcf for 30 min to precipitate the exfoliated CrSBr. The resulting precipitate was washed with tetrahydrofuran (THF, ≥99.9%, inhibitor-free), dried over molecular sieves, transferred into a 20 mL vial, and dried inside an argon-filled glovebox. A dried exfoliated CrSBr sample (3.2 mg) was subsequently subjected to overnight intercalation in 10 mL of 0.64 mM lithium anthracenide solution. To verify the intercalation, the resulting material was dispersed, drop-cast onto a Si/SiO_2 substrate, and characterized by Raman spectroscopy.

4.7 | Magnetic Measurements

Magnetic properties of the Li-intercalated as well as pristine CrSBr samples were studied by SQUID magnetometry in DC fields by employing a Quantum Design (QD) MPMS 3 system. The polycrystalline samples (3.2–18 mg) were mounted into QD capsules for powder samples (≈185 mg) inside a glovebox. Susceptibility was measured in the zero-field-cooled (ZFC) and field-cooled (FC) regimes by applying a probe field of 10 mT. The magnetic response to the applied field was probed by measuring virgin curves and full hysteresis loops at 2 K. For the Li-intercalated sample, an additional hysteresis loop at 2 K was measured upon cooling in the field of 7 T to detect possible exchange bias.

4.8 | AIMD Simulations

We calculated Li^+ diffusion in CrSBr by performing ab initio Born-Oppenheimer molecular dynamics simulations using a Li-intercalated 80-atom supercell ($Li_8Cr_{24}S_{24}Br_{24}$) with 11% lithium intercalation under periodic boundary conditions. Details of the fully relaxed (atomic positions and cell vectors) Li-CrSBr cell are reported in Section S6. The electronic degrees of freedom were dealt with using DFT within the plane-wave pseudopotential formalism (E_{cut} = 40 Ry, GBRV ultrasoft pseudopotentials [37], Brillouin zone integration at the Γ point, and PBEsol exchange-correlation functional [38]). The ions were propagated for 50 ps using an *NVT* ensemble with a stochastic velocity rescaling thermostat [39]. The simulations were performed at temperatures of 600, 800, 1000, and 1200 K using the QUANTUM ESPRESSO software package [34, 35], ver.7.1. The effect of lithium intercalation on the volume was considered by conducting the *NVT* runs on supercells preliminarily equilibrated through *NPT* ensemble simulations for ≈10 ps. The high temperature regime was chosen due to the low mobility of the Li atoms. Total energies and temperatures during these simulations are reported in the Supplementary Information. Diffusion coefficients were extracted from the Li trajectories according to the Einstein relation [26]. Details on the method to extract diffusion coefficients and statistical variances are given in Section S7 and in Ref. [29].

4.9 | TOF-SIMS

Gallium ion source-based FIB-SEM and TOF-SIMS system was used, consisting of the TESCAN LYRA instrument platform and the TOF-SIMS analyzer (TOFWERK AG) developed collaboratively by EMPA (Swiss Federal Laboratories for Materials Science and Technology, Thun) and TESCAN s.r.o. (Brno, CZ). The acquisition was carried out at the ion beam energy of 20 keV and current of 260 pA. Mass count from the scanning area was recorded in 200 × 200 pixel maps with a binning factor of 2 × 2, which eventually resulted in square pixels with a size in *x*- and *y*- dimensions (top side of the crystal) of 200 and 300 nm for scanning view fields of 20 × 20 μm^2 and 30 × 30 μm^2, respectively. The pixel size in the z-direction is 0.1 nm per frame.

Acknowledgements

Z.S. was supported by the European Union's Horizon Europe research and innovation programme under grant agreement ID 101135196. This work was supported by project LUAUS23049 from the Ministry of Education, Youth and Sports (MEYS) and Marie Curie Sklodowska ITN network "2-Exciting" (Grant Number 956813). K.M. acknowledges the grant of specific university research A2 FCHT 2024 055. The authors acknowledge the assistance provided by the Advanced Multiscale Materials for Key Enabling Technologies project, supported by the Ministry of Education, Youth, and Sports of the Czech Republic (project No. CZ.02.01.01/00/22_008/0004558 co-funded by the European Union). M.V. further acknowledges the Czech Science Foundation (GACR No. 23–08083 M) for financial support. Computational resources were provided by the e-INFRA CZ project (ID:90254), supported by the Ministry of Education, Youth and Sports of the Czech Republic. F.D. gratefully acknowledges funding from the Emmy Noether Program (Project-ID 534078167). V.M. and K.M. were supported by project LUAUS23049 from the Ministry of Education Youth and Sports (MEYS). Low temperature experiments were performed in MGML (mgml.eu) supported within the program of Czech Research Infrastructures (project no. LM2023065). Magnetic measurements were carried out within the scope of the TERAFIT project – CZ.02.01.01/00/22_008/0004594, cofounded by the European Union and the Czech Ministry of Education, Youth and Sports. The AIMD simulations work was supported by a grant from the Swiss National Supercomputing Centre (CSCS) under project ID mr33 (Eiger).

Open access publishing facilitated by Vysoka skola chemicko-technologicka v Praze, as part of the Wiley - CzechELib agreement.

Author Contributions

J.S., M.V., and Z.S. initiated and supervised the project. K.M. and Z.S. grew the CrSBr crystals. K.M. and A.S. fabricated heterostructures and performed intercalations as well as Raman measurements. A.S. performed transport measurements. K.M. and A.S. analyzed the data with input from F.D., J.S., M.V. and D.S. G.M., N.M., and G.-M. R. performed molecular dynamics calculations and analyzed the data. J.S. performed DFT calculations. P.L. performed low-temperature transport measurements, O.K. carried out magnetic measurements. M.V. conducted TOF-SIMS analysis. AFM measurements were done by B.R. and V.M. K.M., and A.S. wrote the manuscript with input from all authors.

Conflicts of Interest

The authors declare no conflict of interest.

16163028, 0, Downloaded from https://advanced.onlinelibrary.wiley.com/doi/10.1002/adfm.202523178 by Gian-Marco Rignanese - <shibboleth-member@uclouvain.be> , Wiley Online Library on [17/02/2026]. See the Terms and Conditions (https://onlinelibrary.wiley.com/terms-and-conditions) on Wiley Online Library for rules of use; OA articles are governed by the applicable Creative Commons License

Data Availability Statement

Mosina, K., Luxa, J., & Sofer, Z. (2025). Dataset for Lithium Intercalation in the Anisotropic van der Waals Magnetic Semiconductor CrSBr [Data set]. Zenodo. https://doi.org/10.5281/zenodo.15519716.

References

1. H. Liu, S. Huangfu, X. Zhang, H. Lin, and A. Schilling, "Superconductivity and Charge-Density Wave Formation in Lithium Intercalated 2H-LixTaS$_2$," *Physical Review B* 104 (2021): 064511.

2. J. Luxa, O. Jankovský, D. Sedmidubský, et al., "Origin of Exotic Ferromagnetic Behavior in Exfoliated Layered Transition Metal Dichalcogenides MoS_2 and WS2," *Nanoscale* 8 (2016): 1960–1967.

3. Z. Wang, H. Zheng, and A. Chen, "Room-Temperature CrI3 Magnets through Lithiation," *ACS Nano* 18 (2024): 23058–23066.

4. T. Astles, J. G. McHugh, R. Zhang, et al., "In-Plane Staging in Lithium-Ion Intercalation of Bilayer Graphene," *Nature Communications* 15 (2024): 6933.

5. J. N. Coleman, M. Lotya, and A. O'Neill et al., "Two-Dimensional Nanosheets Produced by Liquid Exfoliation of Layered Materials," *Science* 331 (2011) 568–571.

6. Y. Jung, Y. Zhou, and J. Cha, "Intercalation in Two-Dimensional Transition Metal Chalcogenides," *Inorganic Chemistry Frontiers* 3 (2016): 452–463.

7. M. S. Stark, K. L. Kuntz, S. J. Martens, and S. C. Warren, "Intercalation of Layered Materials from Bulk to 2D," *Advanced Materials* 31 (2019): 1808213.

8. K. Mosina, B. Wu, and N. Antonatos, et al., "Electrochemical Intercalation and Exfoliation of CrSBr into Ferromagnetic Fibers and Nanoribbons," *Small Methods* 8 (2024) 2300609.

9. Y. Wu, J. Wang, and Y. Li, "Observation of an Intermediate State During Lithium Intercalation Of Twisted Bilayer MoS_2," *Nature Communications* 13 (2022): 3008.

10. A. Sagua, E. Morán, and M. A. Alario-Franco, et al., "Lithium Intercalation in FeOCl Revisited," *International Journal of Inorganic Materials* 3 (2001) 293–301.

11. P. Palvadeau, L. Coic, J. Rouxel, and J. Portier, "The Lithium and Molecular Intercalates of FeOCl," *Materials Research Bulletin* 13 (1978) 221–227.

12. T. Yu, X. Zhao, L. Ma, and X. Shen, "Intercalation and Electrochemical Behaviors of Layered FeOCl Cathode Material in Chloride Ion Battery," *Materials Research Bulletin* 96 (2017): 485–490, https://doi.org/10.1016/j.materresbull.2017.03.070.

13. J. Klein, B. Pingault, M. Florian, et al., "The Bulk van der Waals Layered Magnet CrSBr is a Quasi-1D Material," *ACS Nano* 17 (2023): 5316–5328.

14. J. Klein and F. M. Ross, "Materials Beyond monolayers: The magnetic quasi-1D semiconductor CrSBr," *Journal of Materials Research* 39 (2024) 3045–3056.

15. F. Wu, I. Gutiérrez-Lezama, and S. A. López-Paz, et al., "Quasi-1D Electronic Transport in a 2D Magnetic Semiconductor," *Advanced Materials* 34 (2022) 2109759.

16. N. P. Wilson, K. Lee, J. Cenker, et al., "Interlayer Electronic Coupling on Demand in a 2D magnetic Semiconductor," *Nature Materials* 20: 1657–1662 , https://doi.org/10.1038/s41563-021-01070-8.

17. N. Li, M. Dai, Z. Zhao, et al., "Intercalation-Dependent Magnetism in Fe-Intercalated Tantalum Disulfide," *Chemistry of Materials* 37 (2025): 9953–9964.

18. H. Iturriaga, L. M. Martinez, and T. T. Mai, et al., "Magnetic Properties of Intercalated Quasi-2D Fe_3-x$GeTe_2$ Van Der Waals Magnet," *Npj 2D Materials and Applications* 7 (2023): 56.

19. J. M. Pereira, D. Tezze, M. Ormaza, L. E. Hueso, and M. Gobbi, "Engineering Magnetism and Superconductivity in Van Der Waals Materials via Organic-Ion Intercalation," *Advanced Physics Research* 2 (2023): 2200084.

20. M. L. Feuer, M. Thinel, X. Huang, et al., "Charge Density Wave and Ferromagnetism in Intercalated CrSBr," *Advanced Materials* 37 (2025): 2418066.

21. K. Momma and F. Izumi, "VESTA 3 for Three-Dimensional Visualization of Crystal, Volumetric and Morphology Data," *Journal of Applied Crystallography* 44 (2011): 1272–1276.

22. Y. Y. Wang, R. X. Gao, and Z. H. Ni, "Thickness Identification of Two-Dimensional Materials by Optical Imaging," *Nanotechnology* 23 (2012): 495713.

23. Z. Gu, D. Song, and S. Luo, "Insights Into the Anode-Initiated and Grain Boundary-Initiated Mechanisms for Dendrite Formation in All-Solid-State Lithium Metal Batteries *Adv*," *Energy Mater* 13 (2023): 2302945.

24. S. Kim, J. Cui, V. P. Dravid, and K. He, "Orientation-Dependent Intercalation Channels for Lithium and Sodium in Black Phosphorus," *Advanced Materials* 31 (2019): 1904623.

25. C. Zeng, J. Chen, and H. Yang, "Visualizing Fast Interlayer Anisotropic Lithium Diffusion Via Single Crystal Microbattery," *Matter* 5 (2022): 4015–4028.

26. A. Einstein, "Über Die Von Der Molekularkinetischen Theorie Der Wärme Geforderte Bewegung Von In Ruhenden Flüssigkeiten Suspendierten," *Annalen der Physik* 322 (1905) 549–560.

27. D. Chandler, *Introduction to Modern Statistical Mechanics*. (Oxford University Press, 1987).

28. D. Frenkel and B. Smit, *Understanding Molecular Simulation: From Algorithms to Applications*. (Elsevier, 2023).

29. G. Materzanini, L. Kahle, A. Marcolongo, and N. Marzari, "High Li-Ion Conductivity In tetragonal LGPO: A Comparative First-Principles Study Against Known LISICON and LGPS Phases," *Physical Review Materials* 5 (2021): 035408, https://doi.org/10.1103/PhysRevMaterials.5.035408.

30. E. Gilardi, G. Materzanini, L. Kahle, et al., "$Li_{4-x}Ge_{1-x}P_xO_4$, a Potential Solid-State Electrolyte for All-Oxide Microbatteries," *ACS Applied Energy Materials* 3 (2020) 9910–9917.

31. W. Bao, J. Wan, and X. Han, "Approaching the Limits of Transparency and Conductivity in Graphitic Materials Through Lithium Intercalation," *Nature Communications* 5 (2014): 4224.

32. L. Schnitzspan, A. Tries, and M. Kläui, "Electron Transport and the Effect of Current Annealing in a Two-Point Contacted hBN/Graphene/hBN Heterostructure Device," *Journal of Applied Physics* 128: 124302, https://doi.org/10.1063/5.0016471.

33. U. K. Wijewardena, T. Nanayakkara, R. Samaraweera, S. Withanage, A. Kriisa, and R. G. Mani, "Effects of Long-Time Current Annealing to the Hysteresis in CVD Graphene on SiO_2," *MRS Advances* 4 (2019): 3319–3326.

34. P. Giannozzi, O. Andreussi, and T. Brumme, et al., "Advanced Capabilities for Materials Modelling with Quantum ESPRESS," *Journal of Physics: Condensed Matter* 29 (2017): 465901.

35. P. Giannozzi, S. Baroni, and N. Bonini, "QUANTUM ESPRESSO: A Modular and Open-Source Software Project For Quantum Simulations of Materials," *Journal of Physics: Condensed Matter* 21 (2009): 395502.

36. F. Jollet, M. Torrent, and N. Holzwarth, "Generation of Projector Augmented-Wave Atomic Data: A 71 Element Validated Table in the XML Format," *Computer Physics Communications* 185 (2014): 1246–1254, https://doi.org/10.1016/j.cpc.2013.12.023.

37. K. F. Garrity, J. W. Bennett, K. M. Rabe, and D. Vanderbilt, "Pseudopotentials for High-Throughput DFT Calculations," *Computation Materials Science* 81 (2014): 446–452.

38. J. P. Perdew, A. Ruzsinszky, G. I. Csonka, et al., "Restoring the Density-Gradient Expansion for Exchange in Solids and Surfaces," *Physical*

16163028, 0, Downloaded from https://advanced.onlinelibrary.wiley.com/doi/10.1002/adfm.202523178 by Gian-Marco Rignanese - <shibboleth-member@uclouvain.be> , Wiley Online Library on [17/02/2026]. See the Terms and Conditions (https://onlinelibrary.wiley.com/terms-and-conditions) on Wiley Online Library for rules of use; OA articles are governed by the applicable Creative Commons License

Review Letters 100 (2009): 136406, https://doi.org/10.1103/PhysRevLett.100.136406.

39. G. Bussi, D. Donadio, and M. Parrinello, "Canonical Sampling Through Velocity Rescaling," *The Journal of Chemical Physics* 126 (2007): 014101, https://doi.org/10.1063/1.2408420.

Supporting Information

Additional supporting information can be found online in the Supporting Information section.

Supporting File: adfm74033-sup-0001-SuppMat.docx.

Supporting File: adfm74033-sup-0002-VideoS1.mp4.

Supporting File: adfm74033-sup-0003-VideoS2.mp4.

Supporting File: adfm74033-sup-0004-VideoS3.mp4.

Supporting File: adfm74033-sup-0005-VideoS4.mp4.

Supporting File: adfm74033-sup-0006-VideoS5.mp4.

Supporting File: adfm74033-sup-0007-VideoS6.mp4.

16163028, 0, Downloaded from https://advanced.onlinelibrary.wiley.com/doi/10.1002/adfm.202523178 by Gian-Marco Rignanese - <shibboleth>-member@uclouvain.be , Wiley Online Library on [17/02/2026]. See the Terms and Conditions (https://onlinelibrary.wiley.com/terms-and-conditions) on Wiley Online Library for rules of use; OA articles are governed by the applicable Creative Commons License